JACS
JOURNAL OF THE AMERICAN CHEMICAL SOCIETY
pubs.acs.org/JACS
Article

Revealing Solvent-Assisted Li^+ Transport in the Solid Electrolyte Interphase *operando*

Jacob Florian, Hao Lyu, Il Rok Choi, Luca Mondonico, Steven Lam, Yepin Zhao, Min-Jae Kim, Andrew Westover, Yi Cui, Robert L. Sacci,* and Zhenan Bao*

Cite This: *J. Am. Chem. Soc.* 2025, 147, 42701−42710
Read Online
ACCESS | Metrics & More | Article Recommendations | Supporting Information

ABSTRACT: The performance of energy-dense lithium metal batteries is critically influenced by the properties of the solid electrolyte interphase (SEI). Yet, progress in understanding this layer has been limited by the lack of accurate *operando* characterization because the SEI evolves dynamically during cycling. Here, we apply dynamic electrochemical impedance spectroscopy (dEIS) to resolve the real-time evolution of the SEI on lithium metal in ether-based electrolytes with varying degrees of fluorination. We find that faster stabilization of the compact SEI resistance correlates with improved passivation and higher Coulombic efficiency. Unexpectedly, compact SEI resistance correlates directly with Li^+ solvation energy, revealing that weaker Li^+ solvation increases not only bulk but also interphase resistance. These findings challenge the conventional view of the SEI as a purely solid-phase conductor and instead support a solvent-assisted Li^+ transport mechanism within the compact SEI. This framework emphasizes the need to balance SEI ionic conductivity with the Li^+ solvation environment to maximize lithium metal battery performance.

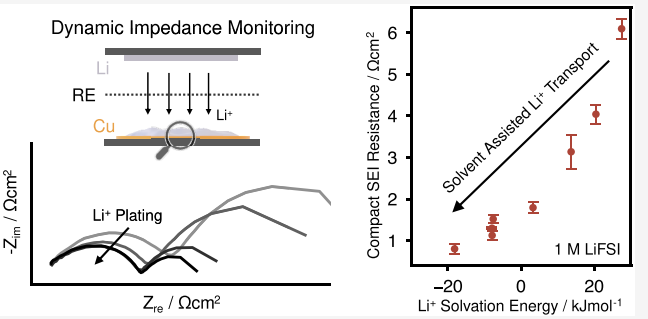

INTRODUCTION

The Li metal anode offers a significant energy density advantage (>500 Wh/kg) over state-of-the-art Li-ion batteries with graphite anodes (300 Wh/kg).[1−3] However, its practical implementation is hindered by Coulombic efficiencies (CE) below the critical 99.9% threshold required for long-term cycling.[4] CE, defined as the ratio of lithium recovered during stripping to lithium deposited during plating, reflects the reversibility of the electrochemical process. Low CE primarily results from the inability to form a fully passivating solid electrolyte interphase (SEI) capable of withstanding the Li metal anode's large volume fluctuations and low electrochemical potential.

Electrolyte engineering is a promising strategy to enhance CE by optimizing SEI formation through the tailored electrolyte properties. An inorganic-rich SEI is generally associated with higher CE,[4−8] but the fundamental Li^+ transport pathways within the SEI and their evolution *operando* remain poorly understood. A deeper understanding of these mechanisms is essential for a rational electrolyte design.

Most SEI models describe a dense, inorganic-rich inner layer—hereafter referred to as the compact SEI—that is impermeable to the electrolyte, facilitating the migration of desolvated Li ions via solid-phase transport.[9−16] In this view, solvent molecules play a minimal role once Li^+ enters the compact SEI. However, experimental validation of SEI properties is challenging due to its extreme sensitivity to environmental conditions. Exposure to air, electron, and X-ray beams, or vacuum can significantly alter its composition and morphology, often leading to misinterpretations of its intrinsic properties.[12,17,18] Moreover, conventional characterization techniques capture only static snapshots, missing the SEI's dynamic evolution during cycling. These limitations have reinforced a common view of the SEI as a passive, ion-conducting barrier rather than a dynamic interphase whose transport properties continuously adapt to interfacial reactions, Li^+ flux, and electrolyte swelling.[18]

Electrochemical impedance spectroscopy (EIS) is one of the few techniques capable of probing SEI properties *operando*.[19−22] However, most EIS studies are performed in two-electrode cells at equilibrium, where the measured response combines contributions from both electrodes. This overlap makes it difficult to isolate the SEI's impedance. Assigning specific impedance features to distinct electrochemical or transport processes is further complicated by the fact that such

Received: August 17, 2025
Revised: October 16, 2025
Accepted: November 4, 2025
Published: November 7, 2025

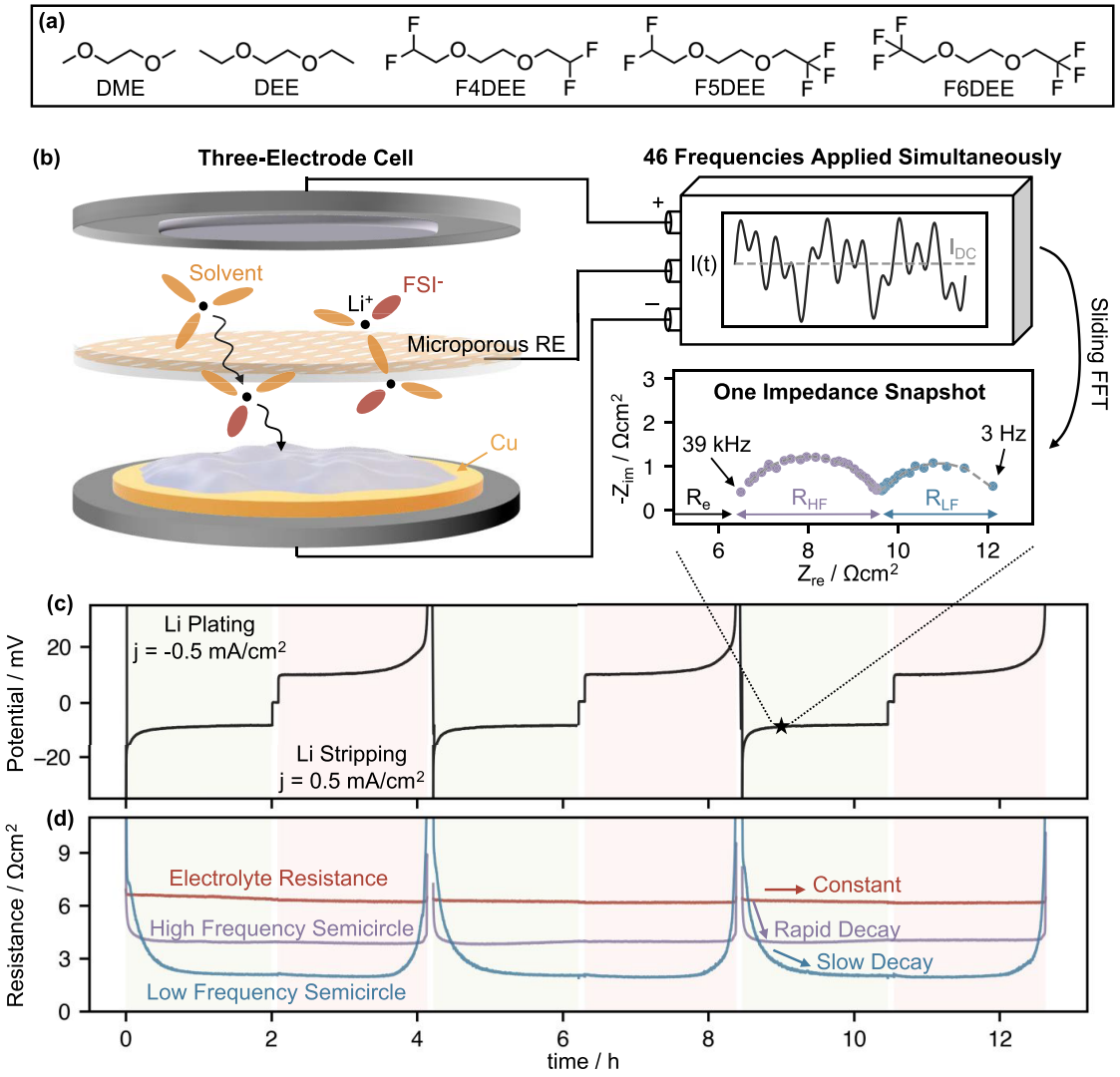

Figure 1. Application of multisine dEIS to study the SEI and its evolution. (a) Solvents used for this study. (b) Scheme showing dEIS application to a 3-electrode coin cell with a microporous reference electrode. A waveform consisting of 46 frequencies is applied simultaneously on top of the DC current. Transforming the voltage response to the frequency domain gives an impedance in real time. One of these impedance snapshots is displayed and fit to extract the values of electrolyte (R_e), high-frequency semicircular resistance (R_{HF}), and low-frequency semicircular resistance (R_{LF}). (c) Cu working electrode voltage trace in 1 M F5DEE for three cycles. (d) Evolution of resistances corresponding to the voltage trace in (c). Resistances are obtained by fitting each impedance snapshot to an R-RQ-RQ equivalent circuit model.

interpretations are usually based on time-constant analysis at equilibrium without systematic evaluation across different cycling conditions.[21,23,24]

In this work, we revisit the interpretation of Li metal interfacial impedance by combining dynamic electrochemical impedance spectroscopy (dEIS) with a three-electrode cell design that isolates the anode's contribution from the bulk Li source. We systematically study its impedance response as a function of time, temperature, electrolyte composition, and applied current and find that it reflects Li^+ transport across two distinct layers: an outer porous layer and an inner compact SEI layer. We find that high CE electrolytes are associated with a rapid decay in compact SEI resistance, indicative of less permeable yet more stable interphases. Notably, we observe a strong correlation between bulk electrolyte solvation energy and compact SEI resistance—evidence for a solvent-assisted Li^+ transport mechanism that challenges the conventional solid-phase conduction model in ether-based electrolytes. These results suggest that tuning the solvation strength and solvent dynamics within the SEI will be essential for optimizing its passivation and ionic conductivity in next-generation electrolytes.

RESULTS AND DISCUSSION

Overview of dEIS Experimental Design. We studied the dynamic impedance behavior of Li metal in a series of ether-based electrolytes (Figure 1a), each containing 1 M lithium bis(fluorosulfonyl)imide (LiFSI), to isolate the effect of solvent chemistry. Impedance was measured with a multisine galvanostatic waveform applied to a three-electrode LiCu coin cell (Figure 1b). This waveform was composed of 46 frequencies (39 kHz to 3 Hz) that were applied simultaneously to the DC current (Figure S1). This enabled time-resolved monitoring of interfacial processes with a resolution defined by the lowest frequency. Benchmark tests showed that spectra collected with this waveform were similar to those obtained with conventional frequency-scanned EIS (Figures S2 and S3), confirming that simultaneous frequency excitation did not

https://doi.org/10.1021/jacs.5c14284
J. Am. Chem. Soc. 2025, 147, 42701−42710

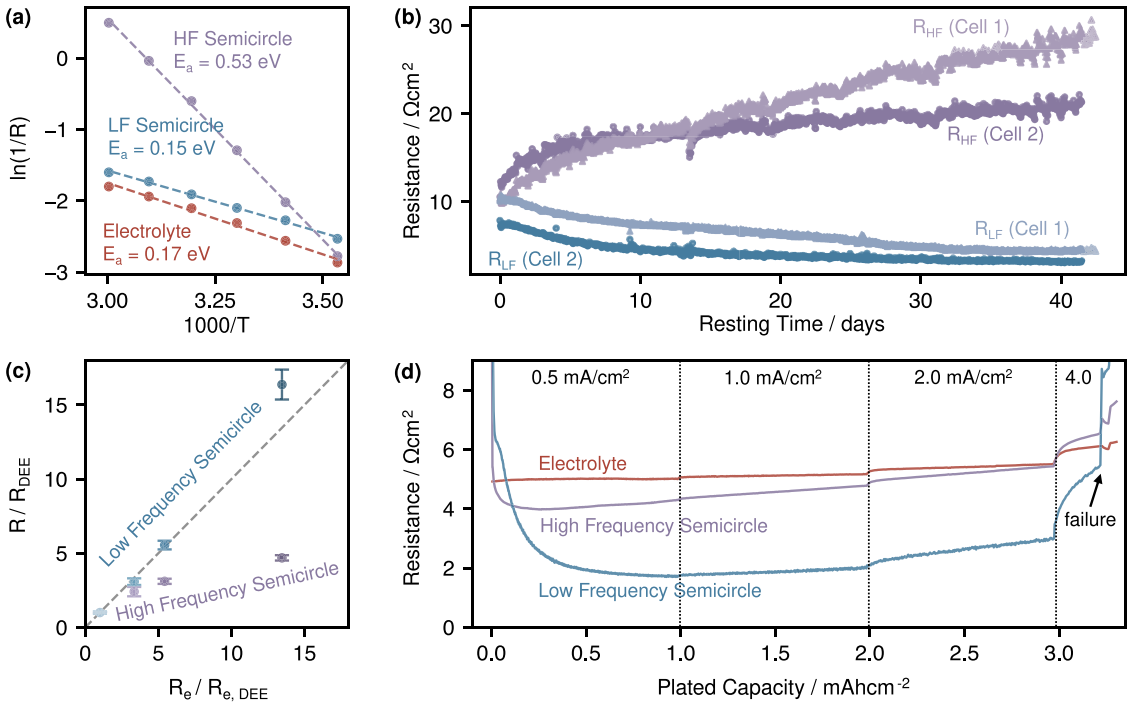

Figure 2. Assigning meaning to cell resistances by examining their response to changes in (a) temperature, (b) time, (c) electrolyte, and (d) applied current density. (a) The apparent activation energy of Li ion conduction in LillLi symmetric cells (1 M LiFSI, F5DEE electrolyte) accomplished by varying the temperature from 10−60 °C. (b) Change in R_{LF} (blue) and R_{HF} (purple) over 40 days of calendar aging in LillLi symmetric cells (1 M LiFSI, F5DEE electrolyte). (c) Semicircular resistances versus electrolyte resistance from dEIS in DEE, F4DEE, F5DEE, and F6DEE (from left to right, 1 M LiFSI). Resistances are normalized by their values in 1 M DEE to show relative change. (d) Cell resistances evolution from dEIS during Li metal plating on a Cu working electrode as the current is increased stepwise from 0.5 to 4 mA/cm^2 (1 M LiFSI, F5DEE electrolyte). All symmetric cells are made using electroplated Li electrodes (0.5 mAcm^{-2}/1 mAhcm^{-2}, see Experimental Methods section for details).

perturb the electrochemical response or induce nonlinear effects.

The three-electrode configuration is critical for isolating the working electrode's impedance during cycling. The reference electrode was made by evaporating Cu onto a Celgard separator to create a conductive, permeable substrate (Figure S4). Before cycling, Li metal was electroplated onto the reference electrode to provide a stable potential throughout the experiment (Figures S5 and S6). Importantly, this microporous reference electrode maintained uniform pressure and electrolyte resistance compared to a standard two-electrode coin cell (Figures S7 and S8) and avoided the instabilities often observed with mesh-type pseudoreference electrodes. Therefore, we were able to monitor both the potential and impedance of the Li metal interface continuously during plating and stripping. This allowed us to track, in real time, the evolution of distinct impedance features and relate them directly to changes in experimental conditions.

The plating and stripping behavior of Li metal was monitored by recording the voltage between the working and reference electrodes during cycling. Figure 1c shows a representative voltage trace for three cycles in 1 M LiFSI in 2-(2-(2,2-difluoroethoxy)ethoxy)-1,1,1-trifluoroethane (F5DEE) as the solvent. F5DEE was tested as it was previously shown to yield >99.5% CE, and its bulk properties can be tuned by the degree of fluorination.[7] In each cycle, the potential is observed to drop sharply during Li plating and stabilizes and reverses direction with a mirrored response during stripping. Notably, the voltage traces for the first three cycles are nearly identical. Unlike standard LillLi cells, where overpotentials are high due to the native SEI and its instability,[25−27] our use of an inert Cu substrate and a reference electrode removes these confounding effects.

In addition to potential, the impedance spectra provided a dynamic view of the interfacial resistance. Each impedance snapshot had two depressed semicircles, which are commonly observed in Li metal anodes.[28−32] To quantify the resistances associated with each semicircle, we fit the impedance spectra to an empirical equivalent circuit containing two RC elements (Figure 1b). Although more complex models exist,[29,33] this simplified model reliably captures the observed resistance changes over time. A time series of impedance spectra is provided as a supplemental movie (Movie S1).

From these fits, we extracted and tracked three resistance components: the electrolyte resistance (R_e), the high-frequency semicircular resistance (R_{HF}), and the low-frequency semicircular resistance (R_{LF}) (Figure 1d). R_e remained stable throughout cycling, indicating no loss of ionic conductivity in the bulk electrolyte. Both semicircular resistances decreased during the early stage of plating, stabilized for most of the cycle, and increased again toward the end of the Li stripping. Notably, the transient decay was much faster for the high-frequency feature than that for the low-frequency feature. R_{HF} stabilized within the first ∼10% of each half-cycle, whereas R_{LF} declined more gradually for the first ∼40% of each half-cycle. This difference in time scales suggests that the two features arise from distinct physical processes.

Assigning Meaning to Impedance Features. To understand the origin of the two semicircular features in Figure 1b, we systematically examined how they responded to

https://doi.org/10.1021/jacs.5c14284
J. Am. Chem. Soc. 2025, 147, 42701−42710

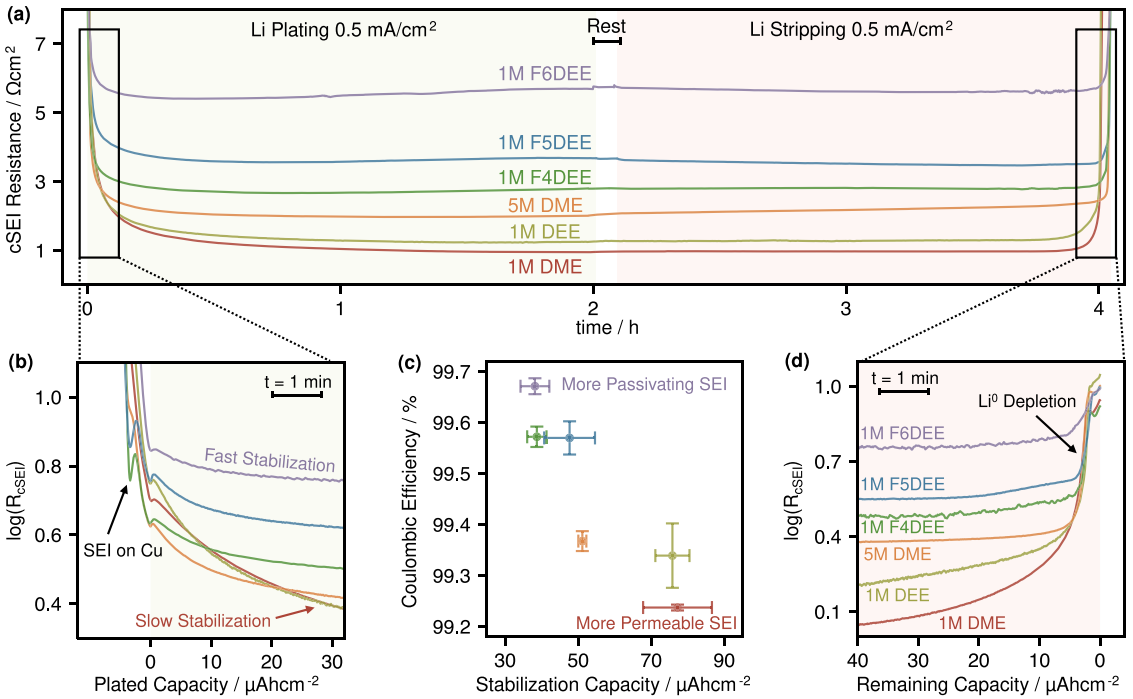

Figure 3. Compact SEI resistance *operando* and its relationship to Coulombic efficiency. (a) Evolution of compact SEI resistance during the first cycle in ether-based electrolytes. (b) Zoomed-in region showing compact SEI resistance during the first 3% of Li metal plating. The zero point marks the start of Li nucleation on Cu. (c) Correlation between the capacity required to achieve SEI stabilization and Aurbach Coulombic efficiency. Stabilization capacity is defined as the capacity at which $\frac{dR_{cSEI}}{dt} < 1\frac{\mu\Omega\ cm^2}{s}$ (Figure S16). (d) Zoomed-in region showing compact SEI resistance during the last 4% of Li metal stripping.

changes in temperature, rest time, electrolyte composition, and applied current density. While EIS is widely used to study Li metal electroplating, there is no consensus on the physical meaning of these features. The high-frequency semicircle is often attributed to Li^+ transport through the SEI in parallel with the SEI's bulk capacitance,[23,25,34,35] but attributing them to charge-transfer resistance or interfacial resistance[36] is also common. The low-frequency semicircle is less clearly defined, with reports linking it to charge transfer,[21,25,37,38] diffusion,[34,39,40] or low-frequency dispersion processes.[28,41,42] Building on foundational work by Aurbach et al.,[34,43] we used controlled variations in experimental conditions to determine which assignments are consistent with the observed trends.

Temperature Dependence. To probe the kinetics of the semicircular features, we performed temperature-dependent impedance measurements in Li|Li symmetric cells using the 1 M F5DEE electrolyte (Figure 2a). Between 10 and 60 °C, the high-frequency resistance exhibited a high apparent activation energy (0.53 eV), indicating a thermally activated process such as ion migration in a dense phase. In contrast, the low-frequency resistance showed a much lower apparent activation energy (0.15 eV), matching that of the bulk electrolyte (0.17 eV) and suggesting Li transport through a medium that is similar mechanistically to the bulk solution.

Calendar Aging. We next examined how the impedance features evolve during the rest. Li|Li symmetric cells were assembled using electrodes prepared by plating 1 mAh of Li in 1 M F5DEE. Over a 40-day resting period, R_{HF} increased continuously while R_{LF} decreased (Figure 2b). These opposing trends occurred over several days, suggesting that the resistance changes reflect structural evolution of the SEI (e.g., thickness and composition changes) rather than transient redistribution of concentration gradients.

Electrolyte Composition. To assess the influence of bulk electrolyte properties, we compared impedance responses in four ether-based electrolytes: 1,2-diethoxyethane (DEE), 1,2-bis(2,2-difluoroethoxy)ethane (F4DEE), F5DEE, and 1,2-bis(2,2,2-trifluoroethoxy)ethane (F6DEE) (Figure 2c). These solvents differ only in fluorine substitution, which affects their bulk properties without drastically altering SEI chemistry or thickness.[7] We observed a near 1:1 correlation between R_{LF} and R_e, implying that the low-frequency semicircle is directly influenced by the bulk electrolyte conductivity. R_{HF} also increased with R_e but did follow a linear 1:1 trend. In the highly conductive 1 M DME electrolyte, the low-frequency semicircle was not discernible (Figure S9).

Applied Current Density. To explore how impedance responds to varying electrochemical driving forces, we performed dEIS measurements during Li plating on Cu at progressively increasing current densities (0.5 to 4 mA/cm²) (Figure 2d). After initial stabilization at 0.5 mA/cm², the current was increased stepwise. Increasing the current from 0.5 to 1 mA/cm² caused no immediate change in either resistance. At 2 and 4 mA/cm², both resistances rose gradually over time, and the electrolyte resistance increased stepwise, consistent with local Li^+ depletion, reducing the bulk ionic conductivity. If either semicircle were dominated by charge transfer resistance (R_{CT}), Butler–Volmer kinetics would predict an immediate drop in resistance with higher overpotential (Note S7).[44,45] However, no such drop was observed. This agrees with prior studies using transient voltammetry that report high exchange current densities (10–100 mA/cm²) in ether-based electrolytes without an SEI.[46–49] Direct comparison of the

https://doi.org/10.1021/jacs.5c14284
J. Am. Chem. Soc. 2025, 147, 42701–42710

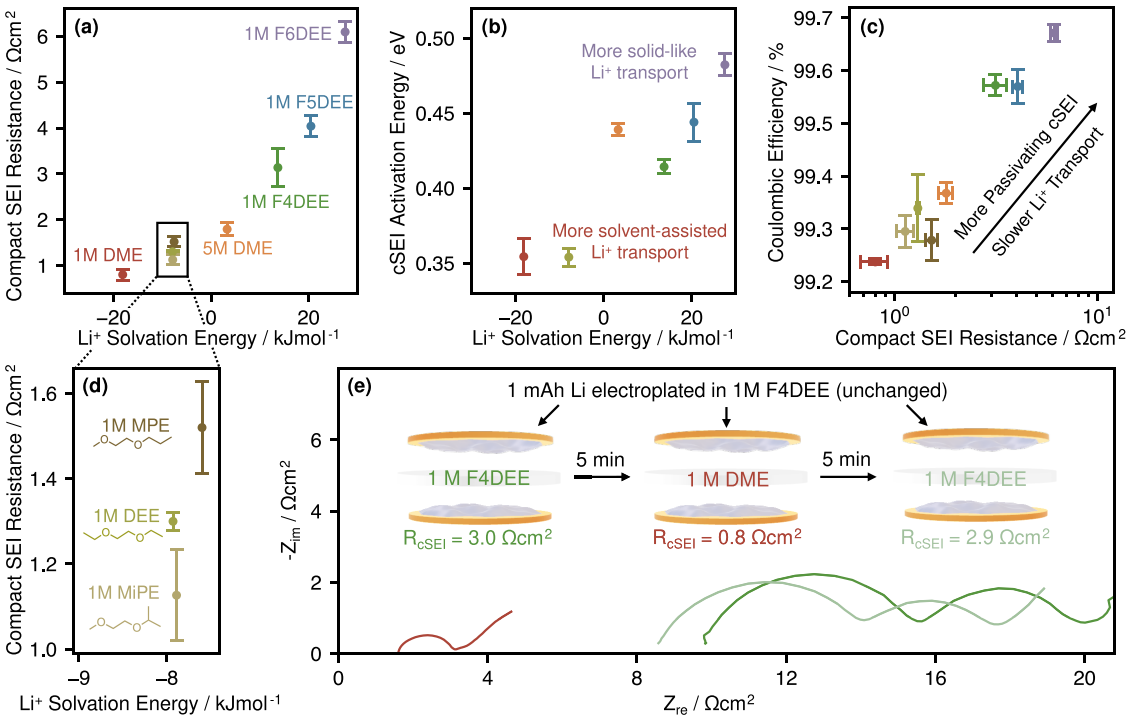

Figure 4. Relationship between compact SEI resistance and electrolyte properties. (a) Compact SEI (cSEI) resistance is correlated to Li^+ solvation energy. There is no correlation between the cSEI resistance and SEI-free exchange current density (Figure S23). (b) Apparent activation energy of Li^+ conduction in the cSEI as a function of Li^+ solvation energy. (c) Correlation between Aurbach Coulombic efficiency and cSEI resistance on a logarithmic scale. (d) Inset for showing variation in cSEI resistance among DEE isomers. (e) Nyquist plots during an electrolyte swap experiment to show the effect of solvent on SEI resistance while controlling SEI composition. A symmetric cell with 1 mAh of Li is electroplated in 1 M F4DEE to form the initial electrodes (dark green). The cell is disassembled, the electrolyte is replaced with 1 M DME (red), and an EIS spectrum is quickly (5 min postassembly) taken. After the final disassembly, 1 M F4DEE is put back into the coin cell (light green).

exchange current densities from transient voltammetry with the semicircular resistances shows no correlation (Figures S23 and S24). These fast intrinsic Li/Li^+ kinetics suggest that Li^+ transport through the SEI, rather than charge transfer at the interface, governs the observed impedance behavior.

Impedance Feature Assignment: Compact and Outer SEI. By combining the above observations, we assign the high-frequency semicircle (R_{HF}) to Li^+ transport through the compact, inner SEI, and the low-frequency semicircle (R_{LF}) to Li^+ diffusion through the porous, outer SEI. No alternative explanation (e.g., charge transfer resistance) can account for all the observed trends.

Specifically, the high apparent activation energy of R_{HF} (0.53 eV) is consistent with ion migration through a dense, passivating layer, while R_{LF}'s apparent activation energy matches that of the bulk electrolyte, reflecting pore-confined diffusion. During rest, R_{HF} should indeed increase as the compact SEI is known to thicken.[36] In contrast, the outer SEI's impedance (R_{LF}) decreases during rest. Possible contributing processes include gradual pore filling from the base upward via electrolyte decomposition, potentially aided by electron leakage,[50] and concurrent dissolution of organic components that shrink the porous interphase and improve pore connectivity.[51] Furthermore, the observation that R_{LF} scales nearly 1:1 with bulk electrolyte resistance is also consistent with electrolyte-filled pores, whereas R_{HF} only partially correlates, reflecting its dependence on both bulk electrolyte and solid-phase transport. Under higher current densities, neither resistance drops instantly, as would be expected for charge transfer, but both rise gradually, which is consistent with the buildup of concentration gradients within the SEI. While the presence of two semicircles does not necessarily indicate only two resistive processes, their evolution with external variables suggests that the primary contribution arises from Li^+ transport through the SEI.

Together, these findings describe a layered SEI in which Li^+ first traverses a dense compact layer (cSEI) before diffusing through a porous outer layer (oSEI) (a schematic representation is shown in Figure 5). The difference in transient decay rates (Figure 1d) naturally follows from this structure: The compact SEI reaches equilibrium faster, whereas the porous outer SEI evolves more slowly as Li plating alters pore volume and connectivity.

Using dEIS to Characterize Compact SEI Evolution in Different Electrolytes. Since the compact SEI resistance (R_{HF}, hereafter R_{cSEI}) is larger than the outer SEI resistance and directly controls Li^+ passivation, we examined how R_{cSEI} evolves in different ether-based electrolytes to identify descriptors for a more stable SEI. Figure 3a shows R_{cSEI} during the first cycle of the Li plating and stripping. While only one dEIS curve is shown per electrolyte, all spectra were reproduced in three independent cells for consistency (Figure S10–S12). In all cases, R_{cSEI} decreased during early plating as the SEI formed, remained steady through most of the cycle, and rose sharply at the end of stripping. However, significant differences emerged in the initial plating and final stripping phases (Figure 3b,d). This observation also highlights the advantages of dEIS, which can capture such dynamic changes in the SEI.

https://doi.org/10.1021/jacs.5c14284
J. Am. Chem. Soc. 2025, 147, 42701−42710

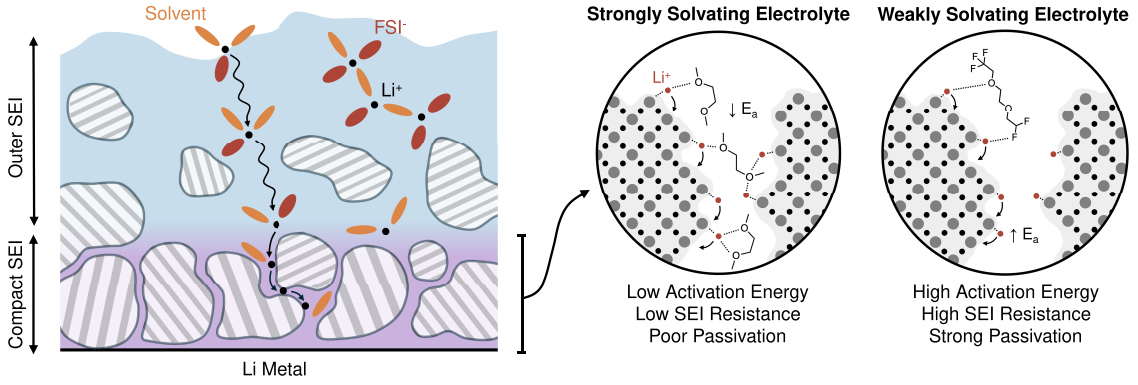

Figure 5. Proposed model of Li^+ transport within the SEI. In the outer SEI, solvated Li ions diffuse through the pores. In the compact SEI, Li^+ migrates along interfacial pathways assisted by solvent interactions. The two insets depict how solvent can assist Li^+ migration along interfaces within the compact SEI depending on the solvation energy. Strongly solvating electrolytes are pulled into the compact SEI, enhancing conductivity. Weakly solvating electrolytes permeate less into the compact SEI, enhancing passivation at the cost of reduced SEI conductivity.

Early Plating and Stabilization. The high temporal resolution of dEIS captures rapid changes in R_{cSEI} before and after Li nucleation on Cu (Figure 3b). Just before nucleation ($Q_{plated} < 0$ μAh), R_{cSEI} drops sharply, reflecting the formation of a primary SEI on Cu (Figure S17). As Li begins to deposit ($0 < Q_{plated} < 100$ μAh), R_{cSEI} approaches a steady value as species in the primary SEI undergo further reduction driven by the presence of metallic Li, such as conversion of alkoxides and other intermediates into more inorganic products.[52] These trends align with previous studies' findings of compositional differences between SEI formed directly on Cu and that formed during Li deposition.[52−54]

The rate at which R_{cSEI} stabilizes varies across electrolytes and correlates with their Coulombic efficiency. To quantify this, we define "stabilization capacity" as the plated capacity for $\frac{dR_{cSEI}}{dt} < 1\frac{\mu\Omega\ cm^2}{s}$, although the trends shown here are not sensitive to that value (Figure S16). Electrolytes with lower stabilization capacities, such as fluorinated ethers, exhibit higher Coulombic efficiency (Figure 3c), consistent with the rapid formation of a more passivating SEI.[7,55] In contrast, 1 M DME and DEE show high stabilization capacities, suggesting that electrolyte permeation into the SEI[18] prolongs decomposition and delays compositional equilibrium.

Changes in the electroactive surface area from Li plating and stripping appear to play a minimal role in compact SEI resistance. There is no correlation between Li coverage and R_{cSEI} (Figure S14), and the capacitance of the compact SEI (C_{cSEI}) is relatively unchanged after Li nucleation (Figure S15). Furthermore, ex-situ SEM images of Li plated in our ether-based electrolytes do not show obvious differences in surface morphology (Figure S25) that would point to significant differences in electroactive surface area between electrolytes. These observations indicate that R_{cSEI} variations arise primarily from intrinsic changes in the SEI conductivity rather than geometry.

Li Stripping. At the end of Li stripping, R_{cSEI} rises sharply, which we hypothesize is a transition from Li stripping to SEI breakdown (Figure 3d). Oxidation of SEI components at more positive potentials likely disrupts Li^+ transport, eventually transforming Cu into a blocking electrode. In fluorinated ethers and 5 M DME, this transition occurs within the last 5 μAh of remaining capacity, just before the Cu potential reaches 1 V. In 1 M DME and DEE, the rise occurs earlier, suggesting less stable passivation and premature SEI degradation.

Solvent-Assisted Li^+ Conduction in the Compact SEI.

The most striking feature in Figure 3a is the large variation in steady state R_{cSEI} values across electrolytes with similar chemistries. R_{cSEI} correlates strongly with both ionic conductivity values (Figure S22) and Li^+ solvation energy (Figure 4a), meaning that bulk electrolyte properties influence ion transport within the compact SEI. This challenges the view that ion conduction occurs purely through solid phases. Supporting this, there is no observable correlation between R_{cSEI} and SEI-free exchange current density[46,49] (Figure S23), confirming that this impedance originates from within the SEI rather than from Li^+ desolvation or charge transfer at the interface.

Although nanoscale pore diffusion has been proposed as a transport mechanism,[56] it is unlikely because rapid electrolyte decomposition near Li metal would block such pores. Instead, our data point toward solvent-assisted transport along interfacial pathways within the multiphasic SEI. Apparent activation energies for Li^+ conduction in the compact SEI range from 0.3 to 0.5 eV (Figures 4b, S18−S20), much higher than bulk electrolyte diffusion (<0.2 eV),[57] indicating thermally activated transport. Electrolytes with stronger solvating power show lower activation energies and lower R_{cSEI}, consistent with an enhanced interfacial transport. Increasing the degree of fluorination, which lowers the solvating ability, raises both R_{cSEI} and activation energy.

Li_2O, a major SEI component, has been shown to adsorb solvated Li^+ ions and facilitate their surface diffusion.[58] In less fluorinated solvents, stronger solvation could enhance such pathways, reducing the R_{cSEI}. To isolate this effect from compositional differences in the SEI, we performed an electrolyte swap experiment (Figure 4e). A Li|Li symmetric cell with an anion-derived[7] SEI formed from electroplating in 1 M F4DEE (R_{cSEI} = 3.0 Ω cm^2) was taken apart and replaced with 1 M DME. After replacing the electrolyte, R_{cSEI} dropped to 0.8 Ω cm^2 despite the same SEI composition. Swapping the electrolyte back to F4DEE restored R_{cSEI} back to 2.9 Ω cm^2, demonstrating that SEI conductivity is reversible and solvent dependent. Although some SEI dissolution or damage is inherent to ex-situ manipulations, the short duration of the electrolyte swap minimizes these effects. Ex-situ XAS further confirmed that the insoluble SEI compositions are identical across the F_xDEE series (Figure S21).

Interestingly, a lower R_{cSEI} does not necessarily yield a higher Coulombic efficiency. Under mild cycling conditions (0.5 mA/

https://doi.org/10.1021/jacs.5c14284
J. Am. Chem. Soc. 2025, 147, 42701−42710

cm^2), higher R_{cSEI} values correlated with better Coulombic efficiency (Figure 4c). This highlights a trade-off: solvent-assisted ion transport improves SEI conductivity but increases solvent interaction with the SEI. This raises the likelihood of undesirable electrolyte decomposition and thus reduces SEI passivation. Conversely, minimizing Li^+ solvation energy with fluorination or high salt concentrations improves SEI passivation but slows Li^+ transport, raising R_{cSEI} and its apparent activation energy, which can limit high-rate performance.

Figure 5 summarizes our proposed mechanism. In the porous outer SEI, solvated Li^+ diffuses through electrolyte-filled pores with bulk-like activation energies. In the compact SEI, a denser structure restricts bulk diffusion, but solvent may still permeate along internal interfaces, reducing the barrier for Li^+ hopping. This effect is strongest in nonfluorinated solvents with high Li^+ affinity. While the structure in Figure 5 is conceptual, cryo-TEM in ether-based electrolytes has been used to observe inorganic domains embedded in an amorphous SEI matrix.[18,59,60] This is consistent with such interfacial pathways, although dEIS offers the advantage of *operando* measurements without structural perturbation.

The balance between compact SEI resistance and passivation defines a clear optimization problem for high-CE Li metal batteries, but it is not the only factor to consider. Structurally similar DEE isomers (MPE and MiPE) show different R_{cSEI} values despite comparable Li^+ solvation energies and bulk electrolyte conductivities (Figure 4d). This suggests molecular geometry can influence solvent swelling into the SEI and interfacial transport, an observation which is supported by advances in asymmetric electrolytes.[49] We propose using low R_{cSEI} together with a low stabilization capacity (Figure 3c) as a design metric for ether-based electrolytes that combine high CE with robust cycling stability.

Our results indicate that Li^+ transport through the compact SEI in ether-based electrolytes is strongly influenced by solvent-assisted pathways. This framework explains several observations that have been difficult to reconcile with conventional solid-state conduction models. The relatively high SEI conductivities we measure, compared to values predicted from individual inorganic components,[41,61−63] are consistent with interfacial transport aided by residual electrolyte. SEI swelling and the accompanying drop in CE[18] align with our finding that strong solvation enhances conductivity but compromises passivation. Likewise, the poor fast-charging performance of weakly solvating fluoroethers[64] may stem from high R_{cSEI}, which promotes concentration gradients and dendrite growth at high rates. Finally, large differences in R_{cSEI} among electrolytes with similar SEI compositions[7] can be explained by variations in solvation environment that can alter the activation energy of Li^+ transport. Collectively, these findings suggest that solvent-assisted ion transport is a general feature of compact SEIs formed in ether-based electrolytes.

CONCLUSION

We used dEIS with a multisine waveform and a three-electrode Li||Cu coin cell to monitor the real-time evolution of the SEI during Li plating and stripping. By decoupling the electrolyte resistance from two distinct semicircular features in the impedance spectra, we identified the high-frequency semicircle (R_{cSEI}) as Li^+ transport through the compact, inner SEI and the low-frequency semicircle (R_{oSEI}) as Li^+ diffusion through the porous, outer SEI. This assignment is supported by consistent trends across temperature, rest time, electrolyte composition, and current density.

Focusing on the compact SEI, we find that the rate at which R_{cSEI} stabilizes during early plating correlates with Coulombic efficiency, providing a practical descriptor for SEI quality. Steady-state R_{cSEI} varies between electrolytes and correlates with their Li^+ solvation energy, indicating that solvent-assisted transport pathways play a key role in ion conduction through the compact SEI. Electrolyte-swap experiments confirm that the SEI conductivity can be reversibly tuned by changing the solvent, independent of SEI composition.

These findings point to a trade-off in the SEI: while weakly solvating electrolytes improve passivation, they also increase SEI resistance. Balancing these effects, potentially through controlled solvent chemistry, molecular geometry, or additive strategies, offers a path toward electrolytes that combine high Coulombic efficiency with fast-charging capability. The descriptors identified here, namely low R_{cSEI} and low stabilization capacity, provide practical targets for guiding electrolyte development for high-performance Li metal batteries.

EXPERIMENTAL METHODS

Materials. LiFSI (99.9%) was purchased from Solvionic. 1,2-Dimethoxyethane (DME, 99.5%) was purchased from Sigma-Aldrich. 1,2-Diethoxyethane (DEE, 99.5%) was purchased from Fischer. 1,2-Bis(2,2-difluoroethoxy)ethane (F4DEE), 2-(2-(2,2-difluoroethoxy)-ethoxy)-1,1,1-trifluoroethane (F5DEE), and 1,2-bis(2,2,2-trifluoroethoxy)ethane (F6DEE) were synthesized according to the reported procedure.[7] 1-Methoxy-2-propoxyethane (MPE) and 1-methoxy-2-(propan-2-yloxy)ethane (MiPE) were synthesized according to the reported procedure.[49] Thick Li chips (600 μm) were purchased from China Energy Lithium. Stainless steel 2032-type coin cell cases, conical springs, and spacers were purchased from MTI.

Three-Electrode Cell Preparation. Li||Cu three-electrode cells were prepared as outlined in sections 3 and 4 in the SI. Briefly, coin cells (2032-type) were made by using Cu foil (1.75 cm^2), a 10 mAh electroplated Li counter electrode (1 cm^2), a Celgard H1409 separator, and an electroplated Li reference electrode. The Cu foil has a ∼5 nm surface coating of Zn to improve the nucleation of Li metal. The reference electrode is made by evaporating 50 nm of Cu onto a Celgard H1409 separator and electroplating 60 μAh of Li metal from the Li counter electrode after cell assembly. The reference wire lead is a 25 μm 316 steel wire insulated with 30 μm thick polypropylene battery tape. 60 μL of each electrolyte was added to each cell.

Symmetric Cell Preparation. All Li||Li symmetric cells were prepared by using electroplated electrodes to eliminate the contribution of passivation layers on commercial Li chips. Two Li||Cu half-cells were assembled in coin cells using a 1 cm^2 Li chip, a 1.75 cm^2 Cu disk, a Celgard 2325 separator, and 44 μL of electrolyte. Each half cell was discharged from its OCV (2−3 V) at a rate of 0.5 mA/cm^2 until the plated capacity of Li reached 1 mAh. Immediately after the plating ceased, the plated half-cells were transferred to an Ar glovebox and disassembled. Then, a new coin cell was assembled using the two 1 mAh electroplated Li on Cu electrodes (one from each half cell) for both the anode and cathode. New casings, springs, spacers, Celgard 2325, and 44 μL of electrolyte were used.

Dynamic Electrochemical Impedance Measurements. Three-electrode Li||Cu cells were discharged from their OCV (2−3 V) with an applied DC current of 0.5 mA/cm^2 until a total capacity of 1 mAh was reached. Then, the cells were charged at 0.5 mA/cm^2 until the cell voltage exceeded 1 V. Between each charge and discharge, the cells were rested for 5 min. On top of the DC current, an ∼15 mV amplitude multisine AC waveform consisting of 46 discrete frequencies ranging from 3 Hz to 39 kHz was added (Table S1). During the measurement, the current and potential were sampled at a

https://doi.org/10.1021/jacs.5c14284
J. Am. Chem. Soc. 2025, 147, 42701−42710

rate of 108 kS/s. A comparison of single- and multisine waveforms is given in Figures S2 and S3. Applying a sliding fast Fourier transform to the transient data produces the real-time complex impedance. The sliding FFT is implemented as described in ref 65. The impedances were fit to an R-RQ-RQ circuit using a Python code interfaced with PyEIS, from which the resulting resistances and equivalent capacitances were calculated.

Coulombic Efficiency Measurements. Coulombic efficiencies of the electrolytes were calculated by using the modified Aurbach method. Two-electrode coin cells were assembled consisting of a Li counter electrode with 10 mAh of electroplated Li and a bare Cu working electrode separated by using Celgard 2325. After resting for 3 h, 5 mAh of Li was plated and stripped from the Cu in an initial formation cycle. Then, 5 mAh of Li was plated to form an initial reservoir. Afterward, Li was stripped and replated 10 times at a capacity of 1 mAh. Finally, the remaining Li was stripped from the Cu. The current density was 0.5 mA/cm^2 for all electrolytes. The Coulombic efficiency was calculated using the following equation.

$$\mathrm{CE} = \frac{Q_{\mathrm{stripped}} + nQ}{Q_{\mathrm{plated}} + nQ} = \frac{Q_{\mathrm{stripped}} + 10}{15}$$

For each electrolyte, the measurement was repeated three times, and the resulting Coulombic efficiencies are tabulated in Table S2. The voltage traces for each electrolyte are also given in Figure S13.

Solvation Energy Measurements. Li ion solvation energies of the electrolytes in this study were measured using the potentiometric method described by Kim.[66] The potential difference between each electrolyte and 1 M LiFSI/DMC was measured using a galvanic cell with Li metal electrodes. Three M LiTFSI in 1:1 DME:DOL (by volume) was used as the salt bridge, and each side of the salt bridge was separated with 4 Celgard 2325 separators. The solvation energy was derived from the open circuit potential using the equation $\Delta G = -\mathrm{FE}_{\mathrm{cell}}$. The solvation energies are given in Table S3 for the three measurements.

Apparent Activation Energy Measurements. The apparent activation energies of Li ion conduction were measured in three-electrode cells by measuring the temperature dependence of the compact SEI resistance. After 1 cycle of dEIS measurements, 1 mAh of Li was plated on the Cu working electrode at 0.5 mA/cm^2, and the cell was equilibrated for 30 min at 0 °C. Afterward, impedance measurements were taken at increments of 10 °C up to 60 °C, with a 20 min equilibration time at each temperature. The temperature was then decreased back to 20 °C to assess the drift of the compact SEI resistance, which was less than 10% in each case. Figures S18 and S19 show the temperature dependence of the Nyquist plots in each electrolyte studied here. To extract activation energies, the compact SEI resistances (measured from the first semicircle) at each temperature were fit to the Arrhenius expression in the following equation.

$$\ln\left(\frac{1}{R_{\mathrm{cSEI}}}\right) = \frac{E_a}{RT} + C$$

The Arrhenius fits were replicated for 2−4 cells in each electrolyte to ensure reproducibility, and the results are shown in Figure S20.

■ ASSOCIATED CONTENT

Supporting Information

The Supporting Information is available free of charge at https://pubs.acs.org/doi/10.1021/jacs.5c14284.

Multisine waveform generation for dEIS, batch fitting of dEIS spectra, reference electrode fabrication, three electrode coin cell assembly, reproducibility of dEIS spectra, comparing multisine with single sine dEIS, note on Butler−Volmer kinetics, Coulombic efficiency calculation, solvation energy calculation, Li coverage during plating, supplemental analysis of dEIS spectra, activation energy for Li^+ conduction in the compact SEI, Ex-situ X-ray absorption spectroscopy of 1 M FxDEE electrolytes, supplemental figures, and references (PDF).

Movie 1 (MP4)

■ AUTHOR INFORMATION

Corresponding Authors

Robert L. Sacci − *Chemical Sciences Division, Oak Ridge National Laboratory, Oak Ridge, Tennessee 37830, United States;* orcid.org/0000-0002-0073-5221; Email: saccirl@ornl.gov

Zhenan Bao − *Department of Chemical Engineering, Stanford University, Stanford, California 94305, United States;* orcid.org/0000-0002-0972-1715; Email: zbao@stanford.edu

Authors

Jacob Florian − *Department of Chemical Engineering, Stanford University, Stanford, California 94305, United States;* orcid.org/0000-0003-1895-8463

Hao Lyu − *Department of Chemical Engineering, Stanford University, Stanford, California 94305, United States*

Il Rok Choi − *Department of Chemical Engineering, Stanford University, Stanford, California 94305, United States; Department of Materials Science and Engineering, Stanford University, Stanford, California 94305, United States*

Luca Mondonico − *Department of Materials Science and Engineering, Stanford University, Stanford, California 94305, United States*

Steven Lam − *Department of Chemical and Biomolecular Engineering, University of Tennessee Knoxville, Knoxville, Tennessee 37996, United States; Chemical Sciences Division, Oak Ridge National Laboratory, Oak Ridge, Tennessee 37830, United States;* orcid.org/0000-0001-5642-9939

Yepin Zhao − *Department of Chemical Engineering, Stanford University, Stanford, California 94305, United States;* orcid.org/0000-0001-9988-0949

Min-Jae Kim − *Advanced Light Source, Lawrence Berkeley National Laboratory, Berkeley, California 94720, United States*

Andrew Westover − *Chemical Sciences Division, Oak Ridge National Laboratory, Oak Ridge, Tennessee 37830, United States*

Yi Cui − *Department of Materials Science and Engineering, Stanford University, Stanford, California 94305, United States;* orcid.org/0000-0002-6103-6352

Complete contact information is available at: https://pubs.acs.org/10.1021/jacs.5c14284

Notes

The authors declare no competing financial interest.

■ ACKNOWLEDGMENTS

This work is supported by the U.S. Department of Energy, under the Assistant Secretary for Energy Efficiency and Renewable Energy, Vehicle Technologies Office, the Battery Materials Research Program, and Battery500 Consortium. SEM imaging was performed at the Stanford Nano Shared Facilities (SNSF), supported by the National Science Foundation under award ECCS-2026822. J.F. acknowledges support from the NSF Graduate Research Fellowship for graduate studies at Stanford. S.L. was supported by the U.S.

Department of Energy, Vehicle Technologies Office under the Silicon Consortium Project, directed by Nicolas Eidson, Carine Steinway, Thomas Do, and Brian Cunningham, and managed by Anthony Burrell. The dEIS instruments and data analyses (R.L.S.) and electrolyte studies (Z.B.) were supported by the U.S. Department of Energy's Vehicle Technologies Office under the U.S.-Germany Energy Storage Consortium, directed by Tien Duong.

REFERENCES

(1) Wang, D.; Qiu, J.; Inui, N.; Hagiwara, R.; Hwang, J.; Matsumoto, K. Between Promise and Practice: A Comparative Look at the Energy Density of Li Metal-Free Batteries and Li Metal Batteries. *ACS Energy Lett.* **2023**, *8* (12), 5248−5252.
(2) Lin, D.; Liu, Y.; Cui, Y. Reviving the Lithium Metal Anode for High-Energy Batteries. *Nat. Nanotechnol.* **2017**, *12* (3), 194−206.
(3) Liu, J.; Xiao, J.; Yang, J.; Wang, W.; Shao, Y.; Liu, P.; Whittingham, M. S. The TWh Challenge: Next Generation Batteries for Energy Storage and Electric Vehicles. *Energy* **2023**, *1* (1), No. 100015.
(4) Zhao, Y.; Zhou, T.; Mensi, M.; Choi, J. W.; Coskun, A. Electrolyte Engineering via Ether Solvent Fluorination for Developing Stable Non-Aqueous Lithium Metal Batteries. *Nat. Commun.* **2023**, *14* (1), No. 299.
(5) Zhao, Y.; Zhou, T.; Jeurgens, L. P. H.; Kong, X.; Choi, J. W.; Coskun, A. Electrolyte Engineering for Highly Inorganic Solid Electrolyte Interphase in High-Performance Lithium Metal Batteries. *Chem.* **2023**, *9* (3), 682−697.
(6) Wang, H.; Yu, Z.; Kong, X.; Kim, S. C.; Boyle, D. T.; Qin, J.; Bao, Z.; Cui, Y. Liquid Electrolyte: The Nexus of Practical Lithium Metal Batteries. *Joule* **2022**, *6* (3), 588−616.
(7) Yu, Z.; Rudnicki, P. E.; Zhang, Z.; Huang, Z.; Celik, H.; Oyakhire, S. T.; Chen, Y.; Kong, X.; Kim, S. C.; Xiao, X.; Wang, H.; Zheng, Y.; Kamat, G. A.; Kim, M. S.; Bent, S. F.; Qin, J.; Cui, Y.; Bao, Z. Rational Solvent Molecule Tuning for High-Performance Lithium Metal Battery Electrolytes. *Nat. Energy* **2022**, *7* (1), 94−106.
(8) Sun, Y.; Li, J.; Xu, S.; Zhou, H.; Guo, S. Molecular Engineering toward Robust Solid Electrolyte Interphase for Lithium Metal Batteries. *Adv. Mater.* **2024**, *36* (14), No. 2311687.
(9) Shi, S.; Lu, P.; Liu, Z.; Qi, Y.; Hector, L. G., Jr.; Li, H.; Harris, S. J. Direct Calculation of Li-Ion Transport in the Solid Electrolyte Interphase. *J. Am. Chem. Soc.* **2012**, *134* (37), 15476−15487.
(10) Zhou, Y.; Su, M.; Yu, X.; Zhang, Y.; Wang, J.-G.; Ren, X.; Cao, R.; Xu, W.; Baer, D. R.; Du, Y.; Borodin, O.; Wang, Y.; Wang, X.-L.; Xu, K.; Xu, Z.; Wang, C.; Zhu, Z. Real-Time Mass Spectrometric Characterization of the Solid−Electrolyte Interphase of a Lithium-Ion Battery | Nature Nanotechnology. *Nat. Nanotechnol.* **2020**, *15* (3), 224−230.
(11) Ramasubramanian, A.; Yurkiv, V.; Foroozan, T.; Ragone, M.; Shahbazian-Yassar, R.; Mashayek, F. Lithium Diffusion Mechanism through Solid−Electrolyte Interphase in Rechargeable Lithium Batteries. *J. Phys. Chem. C* **2019**, *123* (16), 10237−10245.
(12) Sun, S.-Y.; Zhang, X.-Q.; Wang, Y.-N.; Li, J.-L.; Zheng, Z.; Huang, J.-Q. Understanding the Transport Mechanism of Lithium Ions in Solid-Electrolyte Interphase in Lithium Metal Batteries with Liquid Electrolytes. *Mater. Today* **2024**, *77*, 39−65.
(13) Benitez, L.; Seminario, J. M. Ion Diffusivity through the Solid Electrolyte Interphase in Lithium-Ion Batteries. *J. Electrochem. Soc.* **2017**, *164* (11), No. E3159.
(14) Williams, B. P.; Zhang, H.; Mu, Y.; Wilkes, J. R.; Wikar, H.; Wang, D. Li+ Ion Transport at the Lithium Metal Anode: A Fundamental Picture and Future Perspectives. *J. Phys. Chem. C* **2022**, *126* (26), 10644−10652.
(15) Hess, M. Non-Linearity of the Solid-Electrolyte-Interphase Overpotential. *Electrochim. Acta* **2017**, *244*, 69−76.
(16) Soto, F. A.; Marzouk, A.; El-Mellouhi, F.; Balbuena, P. B. Understanding Ionic Diffusion through SEI Components for Lithium-Ion and Sodium-Ion Batteries: Insights from First-Principles Calculations. *Chem. Mater.* **2018**, *30* (10), 3315−3322.
(17) Yu, W.; Yu, Z.; Cui, Y.; Bao, Z. Degradation and Speciation of Li Salts during XPS Analysis for Battery Research. *ACS Energy Lett.* **2022**, *7* (10), 3270−3275.
(18) Zhang, Z.; Li, Y.; Xu, R.; Zhou, W.; Li, Y.; Oyakhire, S. T.; Wu, Y.; Xu, J.; Wang, H.; Yu, Z.; Boyle, D. T.; Huang, W.; Ye, Y.; Chen, H.; Wan, J.; Bao, Z.; Chiu, W.; Cui, Y. Capturing the Swelling of Solid-Electrolyte Interphase in Lithium Metal Batteries. *Science* **2022**, *375* (6576), 66−70.
(19) Drvarič Talian, S.; Kapun, G.; Moškon, J.; Dominko, R.; Gaberšček, M. *Operando* Impedance Spectroscopy with Combined Dynamic Measurements and Overvoltage Analysis in Lithium Metal Batteries. *Nat. Commun.* **2025**, *16* (1), No. 2030.
(20) Kitz, P. G.; Lacey, M. J.; Novák, P.; Berg, E. J. *Operando* EQCM-D with Simultaneous in Situ EIS: New Insights into Interphase Formation in Li Ion Batteries. *Anal. Chem.* **2019**, *91* (3), 2296−2303.
(21) Cho, C.-S.; Wu, Y.-W.; Liao, M.-W.; Chen, J.-K.; Li, C.-C. In-Situ Analysis of Cathode and Anode Impedances to Probe the Performance Degradation of Lithium−Sulfur Batteries. *J. Power Sources* **2024**, *620*, No. 235235.
(22) Hu, W.; Peng, Y.; Wei, Y.; Yang, Y. Application of Electrochemical Impedance Spectroscopy to Degradation and Aging Research of Lithium-Ion Batteries. *J. Phys. Chem. C* **2023**, *127* (9), 4465−4495.
(23) Talian, S. D.; Brutti, S.; Navarra, M. A.; Moškon, J.; Gaberscek, M. Impedance Spectroscopy Applied to Lithium Battery Materials: Good Practices in Measurements and Analyses. *Energy Storage Mater.* **2024**, *69*, No. 103413.
(24) Lang, S.; Colletta, M.; Krumov, M. R.; Seok, J.; Kourkoutis, L. F.; Wen, R.; Abruña, H. D. Multidimensional Visualization of the Dynamic Evolution of Li Metal via in Situ/*Operando* Methods. *Proc. Natl. Acad. Sci. U. S. A.* **2023**, *120* (7), No. e2220419120.
(25) Srout, M.; Carboni, M.; Gonzalez, J.-A.; Trabesinger, S. Insights into the Importance of Native Passivation Layer and Interface Reactivity of Metallic Lithium by Electrochemical Impedance Spectroscopy. *Small* **2023**, *19* (7), No. 2206252.
(26) Wood, K. N.; Kazyak, E.; Chadwick, A. F.; Chen, K.-H.; Zhang, J.-G.; Thornton, K.; Dasgupta, N. P. Dendrites and Pits: Untangling the Complex Behavior of Lithium Metal Anodes through *Operando* Video Microscopy. *ACS Cent. Sci.* **2016**, *2* (11), 790−801.
(27) Koo, D.; Kwon, B.; Lee, J.; Lee, K. T. Asymmetric Behaviour of Li/Li Symmetric Cells for Li Metal Batteries. *Chem. Commun.* **2019**, *55* (65), 9637−9640.
(28) Jamnik, J.; Gaberšček, M.; Meden, A.; Pejovnik, S. Space-Charge at the Lithium-Lithium Chloride Interface. *J. Electrochem. Soc.* **1991**, *138* (6), No. 1582.
(29) Drvarič Talian, S.; Bobnar, J.; Sinigoj, A. R.; Humar, I.; Gaberšček, M. Transmission Line Model for Description of the Impedance Response of Li Electrodes with Dendritic Growth. *J. Phys. Chem. C* **2019**, *123* (46), 27997−28007.
(30) Thevenin, J. Passivating Films on Lithium Electrodes. An Approach by Means of Electrode Impedance Spectroscopy. *J. Power Sources* **1985**, *14* (1), 45−52.
(31) Gaberšček, M. Understanding Li-Based Battery Materials via Electrochemical Impedance Spectroscopy. *Nat. Commun.* **2021**, *12* (1), No. 6513.
(32) Takami, N.; Ohsaki, T.; Inada, K. The Impedance of Lithium Electrodes in LiPF6 - Based Electrolytes. *J. Electrochem. Soc.* **1992**, *139* (7), No. 1849.
(33) Single, F.; Horstmann, B.; Latz, A. Theory of Impedance Spectroscopy for Lithium Batteries. *J. Phys. Chem. C* **2019**, *123* (45), 27327−27343.
(34) Zaban, A.; Zinigrad, E.; Aurbach, D. Impedance Spectroscopy of Li Electrodes. 4. A General Simple Model of the Li−Solution Interphase in Polar Aprotic Systems. *J. Phys. Chem. A* **1996**, *100* (8), 3089−3101.

(35) Zhou, B.; Stoševski, I.; Bonakdarpour, A.; Wilkinson, D. P. Decoupling of the Impedance of Solid-Electrolyte Interface and Plated Lithium: Implications for Anode-Free Lithium Metal Battery Technology. *ACS Appl. Energy Mater.* **2023**, *6* (13), 6890−6895.
(36) Boyle, D. T.; Huang, W.; Wang, H.; Li, Y.; Chen, H.; Yu, Z.; Zhang, W.; Bao, Z.; Cui, Y. Corrosion of Lithium Metal Anodes during Calendar Ageing and Its Microscopic Origins. *Nat. Energy* **2021**, *6* (5), 487−494.
(37) Zhang, S. S.; Xu, K.; Jow, T. R. EIS Study on the Formation of Solid Electrolyte Interface in Li-Ion Battery. *Electrochim. Acta* **2006**, *51* (8), 1636−1640.
(38) Yin, X.; Li, B.; Liu, H.; Wen, B.; Liu, J.; Bai, M.; Zhang, Y.; Zhao, Y.; Cui, X.; Su, Y.; Gao, G.; Ding, S.; Yu, W. Solvent-Derived Organic-Rich SEI Enables Capacity Enhancement for Low-Temperature Lithium Metal Batteries. *Joule* **2025**, *9* (4), No. 101823, DOI: 10.1016/j.joule.2025.101823.
(39) Gaberščček, M.; Pejovnik, S. Time Evolution of the Impedance Response of a Passive Film: A Simple Application to the Li/SOCl2 System. *J. Electrochem. Soc.* **1999**, *146* (3), No. 933.
(40) Churikov, A. V.; Nimon, E. S.; Lvov, A. L. Impedance of Li-Sn, Li-Cd and Li-Sn-Cd Alloys in Propylene Carbonate Solution. *Electrochim. Acta* **1997**, *42* (2), 179−189.
(41) Gaberščček, M.; Jamnik, J.; Pejovnik, S. Impedance Spectroscopy of a Passive Layer on Lithium. *J. Electrochem. Soc.* **1993**, *140* (2), No. 308.
(42) Jonscher, A. K. Admittance Spectroscopy of Systems Showing Low-Frequency Dispersion. *Electrochim. Acta* **1990**, *35* (10), 1595−1600.
(43) Aurbach, D.; Zaban, A. Impedance Spectroscopy of Lithium Electrodes: Part 1. General Behavior in Propylene Carbonate Solutions and the Correlation to Surface Chemistry and Cycling Efficiency. *J. Electroanal. Chem.* **1993**, *348* (1), 155−179.
(44) Self, E. C.; Delnick, F. M.; Sacci, R. L.; Nanda, J. Assessing Nonlinear Polarization in Electrochemical Cells Using AC Impedance Spectroscopy. *J. Electrochem. Soc.* **2024**, *171* (3), No. 030513.
(45) Stolz, L.; Winter, M.; Kasnatscheew, J. Practical Relevance of Charge Transfer Resistance at the Li Metal Electrodelelectrolyte Interface in Batteries? *J. Solid State Electrochem.* **2025**, *29*, 4181−4186.
(46) Boyle, D. T.; Kong, X.; Pei, A.; Rudnicki, P. E.; Shi, F.; Huang, W.; Bao, Z.; Qin, J.; Cui, Y. Transient Voltammetry with Ultramicroelectrodes Reveals the Electron Transfer Kinetics of Lithium Metal Anodes. *ACS Energy Lett.* **2020**, *5* (3), 701−709.
(47) Hobold, G. M.; Kim, K.-H.; Gallant, B. M. Beneficial vs. Inhibiting Passivation by the Native Lithium Solid Electrolyte Interphase Revealed by Electrochemical Li+ Exchange. *Energy Environ. Sci.* **2023**, *16* (5), 2247−2261.
(48) Aojula, K. S.; Genders, J. D.; Holding, A. D.; Pletcher, D. Application of Microelectrodes to the Study of the Li/Li+ Couple in Ether Solvents—III. *Electrochim. Acta* **1989**, *34* (11), 1535−1539.
(49) Choi, I. R.; Chen, Y.; Shah, A.; Florian, J.; Serrao, C.; Holoubek, J.; Lyu, H.; Zhang, E.; Lee, J. H.; Lin, Y.; Kim, S. C.; Park, H.; Zhang, P.; Lee, J.; Qin, J.; Cui, Y.; Bao, Z. Asymmetric Ether Solvents for High-Rate Lithium Metal Batteries. *Nat. Energy* **2025**, *10*, 1−15.
(50) Köbbing, L.; Latz, A.; Horstmann, B. Growth of the Solid-Electrolyte Interphase: Electron Diffusion versus Solvent Diffusion. *J. Power Sources* **2023**, *561*, No. 232651.
(51) Sayavong, P.; Zhang, W.; Oyakhire, S. T.; Boyle, D. T.; Chen, Y.; Kim, S. C.; Vilá, R. A.; Holmes, S. E.; Kim, M. S.; Bent, S. F.; Bao, Z.; Cui, Y. Dissolution of the Solid Electrolyte Interphase and Its Effects on Lithium Metal Anode Cyclability. *J. Am. Chem. Soc.* **2023**, *145* (22), 12342−12350.
(52) Gu, Y.; You, E.-M.; Lin, J.-D.; Wang, J.-H.; Luo, S.-H.; Zhou, R.-Y.; Zhang, C.-J.; Yao, J.-L.; Li, H.-Y.; Li, G.; Wang, W.-W.; Qiao, Y.; Yan, J.-W.; Wu, D.-Y.; Liu, G.-K.; Zhang, L.; Li, J.-F.; Xu, R.; Tian, Z.-Q.; Cui, Y.; Mao, B.-W. Resolving Nanostructure and Chemistry of Solid-Electrolyte Interphase on Lithium Anodes by Depth-Sensitive Plasmon-Enhanced Raman Spectroscopy. *Nat. Commun.* **2023**, *14* (1), No. 3536.
(53) Menkin, S.; O'Keefe, C. A.; Gunnarsdóttir, A. B.; Dey, S.; Pesci, F. M.; Shen, Z.; Aguadero, A.; Grey, C. P. Toward an Understanding of SEI Formation and Lithium Plating on Copper in Anode-Free Batteries. *J. Phys. Chem. C* **2021**, *125* (30), 16719−16732.
(54) Lin, D.; Liu, Y.; Li, Y.; Li, Y.; Pei, A.; Xie, J.; Huang, W.; Cui, Y. Fast Galvanic Lithium Corrosion Involving a Kirkendall-Type Mechanism. *Nat. Chem.* **2019**, *11* (4), 382−389.
(55) Qian, J.; Henderson, W. A.; Xu, W.; Bhattacharya, P.; Engelhard, M.; Borodin, O.; Zhang, J.-G. High Rate and Stable Cycling of Lithium Metal Anode. *Nat. Commun.* **2015**, *6* (1), No. 6362.
(56) Yu, Y.; Koh, H.; Zhang, Z.; Yang, Z.; Alexandrova, A. N.; Agarwal, M.; Stach, E. A.; Xie, J. Kinetic Pathways of Fast Lithium Transport in Solid Electrolyte Interphases with Discrete Inorganic Components. *Energy Environ. Sci.* **2023**, *16* (12), 5904−5915.
(57) Jow, T. R.; Delp, S. A.; Allen, J. L.; Jones, J.-P.; Smart, M. C. Factors Limiting Li+ Charge Transfer Kinetics in Li-Ion Batteries. *J. Electrochem. Soc.* **2018**, *165* (2), No. A361.
(58) Kim, M. S.; Zhang, Z.; Rudnicki, P. E.; Yu, Z.; Wang, J.; Wang, H.; Oyakhire, S. T.; Chen, Y.; Kim, S. C.; Zhang, W.; Boyle, D. T.; Kong, X.; Xu, R.; Huang, Z.; Huang, W.; Bent, S. F.; Wang, L.-W.; Qin, J.; Bao, Z.; Cui, Y. Suspension Electrolyte with Modified Li+ Solvation Environment for Lithium Metal Batteries. *Nat. Mater.* **2022**, *21* (4), 445−454.
(59) Han, B.; Li, X.; Bai, S.; Zou, Y.; Lu, B.; Zhang, M.; Ma, X.; Chang, Z.; Meng, Y. S.; Gu, M. Conformal Three-Dimensional Interphase of Li Metal Anode Revealed by Low-Dose Cryoelectron Microscopy. *Matter* **2021**, *4* (11), 3741−3752.
(60) Wi, T.-U.; Park, S. O.; Yeom, S. J.; Kim, M.-H.; Kristanto, I.; Wang, H.; Kwak, S. K.; Lee, H.-W. Revealing the Dual-Layered Solid Electrolyte Interphase on Lithium Metal Anodes via Cryogenic Electron Microscopy. *ACS Energy Lett.* **2023**, *8* (5), 2193−2200.
(61) Guo, R.; Gallant, B. M. Li2O Solid Electrolyte Interphase: Probing Transport Properties at the Chemical Potential of Lithium. *Chem. Mater.* **2020**, *32* (13), 5525−5533.
(62) Lorger, S.; Narita, K.; Usiskin, R.; Maier, J. Enhanced Ion Transport in Li2O and Li2S Films. *Chem. Commun.* **2021**, *57* (53), 6503−6506.
(63) Lorger, S.; Usiskin, R.; Maier, J. Transport and Charge Carrier Chemistry in Lithium Oxide. *J. Electrochem. Soc.* **2019**, *166* (10), No. A2215.
(64) Chen, Y.; Yu, Z.; Gong, H.; Zhang, W.; Rudnicki, P. E.; Huang, Z.; Yu, W.; Kim, S. C.; Boyle, D. T.; Sayavong, P.; Celik, H.; Xu, R.; Lin, Y.; Wang, S.; Qin, J.; Cui, Y.; Bao, Z. Failure Process During Fast Charging of Lithium Metal Batteries with Weakly Solvating Fluoroether Electrolytes. *J. Phys. Chem. C* **2024**, *128* (28), 11487−11497.
(65) Sacci, R. L.; Seland, F.; Harrington, D. A. Dynamic Electrochemical Impedance Spectroscopy, for Electrocatalytic Reactions. *Electrochim. Acta* **2014**, *131*, 13−19.
(66) Kim, S. C.; Kong, X.; Vilá, R. A.; Huang, W.; Chen, Y.; Boyle, D. T.; Yu, Z.; Wang, H.; Bao, Z.; Qin, J.; Cui, Y. Potentiometric Measurement to Probe Solvation Energy and Its Correlation to Lithium Battery Cyclability. *J. Am. Chem. Soc.* **2021**, *143* (27), 10301−10308.